


Three-dimensional instabilities of natural convection between two differentially heated vertical plates: Linear and nonlinear complementary approaches

Zhenlan Gao,^{1,2,3,*} Berengere Podvin,^{1,†} Anne Sergent,^{1,2} Shihe Xin,⁴ and Jalel Chergui¹
¹*LIMSI, CNRS, Université Paris-Saclay, Campus Universitaire, rue Von Neumann, 91400 Orsay, France*
²*Sorbonne Université, Faculté des Sciences et Ingénierie, UFR d'Ingénierie, F-75005 Paris, France*
³*ECM Technologies, 46 rue Jean Vaujany, 38100 Grenoble, France*
⁴*CETHIL, INSA de Lyon, 69621 Villeurbanne Cedex, France*

 (Received 30 January 2018; revised manuscript received 24 April 2018; published 22 May 2018)

The transition to the chaos of the air flow between two vertical plates maintained at different temperatures is studied in the Boussinesq approximation. After the first bifurcation at critical Rayleigh number Ra_c , the flow consists of two-dimensional (2D) corotating rolls. The stability of the 2D rolls is examined, confronting linear predictions with nonlinear integration. In all cases the 2D rolls are destabilized in the spanwise direction. Efficient linear stability analysis based on an Arnoldi method shows competition between two eigenmodes, corresponding to different spanwise wavelengths and different types of roll distortion. Nonlinear integration shows that the lower-wave-number mode is always dominant. A partial route to chaos is established through the nonlinear simulations. The flow becomes temporally chaotic for $Ra = 1.05Ra_c$, but remains characterized by the spatial patterns identified by linear stability analysis. This highlights the complementary role of linear stability analysis and nonlinear simulation.

DOI: [10.1103/PhysRevE.97.053107](https://doi.org/10.1103/PhysRevE.97.053107)

I. INTRODUCTION

Natural convection between two infinite vertical differentially heated plates is an idealized configuration of interest for a large range of geophysical or industrial applications such as water pollution, insulation, or cooling of electronic devices. In order to minimize the energy expense and enhance the transfer properties of these processes, which are generally complex, it is important to achieve a thorough understanding of the instability mechanisms in simplified geometries. The focus of the current paper is the early transition of the flow, which shares some similarities with that of a confined mixing layer, and not the fully turbulent boundary layer regime. The idea is to map out the first instabilities leading the flow to chaos.

Several earlier studies have been carried out in two-dimensional (2D) configuration [1–20], however these studies leave out potentially important three-dimensional (3D) effects. One of our goals is to carry out three-dimensional stability analysis of the natural convection between two infinite, vertical, differentially heated plates, following an approach recently used for other three-dimensional geometries, such as a cubic cavity [21], as well as in a horizontal cylinder in the presence of rotation [22].

In the vertical fluid layer, a few studies have already partially investigated the sequence of instabilities in three dimensions and brought to light the destabilizing effect of spanwise modes. In these studies the Prandtl number defined as $Pr = \nu/\kappa$, where ν is the kinematic viscosity and κ is the thermal diffusivity, is fixed and the varying parameter is the Rayleigh number

defined as $Ra = g\beta\Delta TD^3/(\nu\kappa)$, with β the thermal expansion coefficient, g the gravity, ΔT the temperature difference, and D the distance between the plates. The pioneering study of Nagata and Busse [23] investigated the sequence of instabilities in a shear layer between two differentially heated sidewalls in the limit of $Pr = 0$. The primary instability consisted of 2D transverse rolls. Three secondary instability mechanisms for the rolls were identified: an Eckhaus instability in the vertical direction, a monotone instability, and an oscillatory instability. Above the Rayleigh number $Ra = 5822$, the 2D flow bifurcates to a steady 3D pattern corresponding to “a vortex-pairing instability with alternating pairing in the spanwise direction” [23]. This 3D pattern becomes unstable when $Ra > 7852$ and gives way to an oscillatory 3D pattern, which corresponds to structures shifted back and forth periodically in time in the transverse direction. The spanwise wavelength of the structures is twice that of the steady pattern associated with the monotone instability.

Chait and Korpela [24] also studied the stability of 2D rolls for air ($Pr = 0.71$) convection between two vertical differentially heated plates. Since Pr is not zero, the stability map is somewhat different from Nagata and Busse’s [23], although they do recover the three types of instabilities found by these authors. They denote the first monotone instability A. However they also identify a second monotone instability, which they denote B. The pattern associated with instability B consists of rolls periodically thickening and thinning in the transverse direction y , which resembles the skewed varicose instability in Rayleigh-Bénard convection.

Still another study by Clever and Busse [25] computed equilibria and traveling wave solutions for air convection between two vertical differentially heated plates. They also recovered the monotone instability A. Using symmetry

*z.gao@ecmtech.fr

†podvin@limsi.fr

considerations, other possible solutions were charted at different Rayleigh numbers. They brought to light a pattern consisting of a traveling wave of 3D invariant shape moving downward, which is different from the oscillatory flow pattern found by Nagata and Busse [23]. Both the instability A and the traveling wave modes were found to exist at $Ra = 7000$. This is in partial agreement with Wright *et al.*'s experiment in air [26], which displayed 2D rolls at $Ra = 6800$ moving slowly downwards. Two-dimensional rolls moving slowly downwards were also identified in the experimental results and the 2D numerical simulation of Lartigue *et al.* [20] in a tall air-filled cavity.

Although similar 3D instability mechanisms were identified in these three studies, it is not known which solutions are actually found in the flow. To determine this, three-dimensional direct numerical simulation (DNS) was carried out for the air flow between two infinite, vertical, differentially heated plates [27]. Due to the computational cost, the spanwise periodic dimension of the domain was constrained to be equal to the interplate distance. Successive flow bifurcations were investigated from the one-dimensional base flow to the 3D chaotic regime. As predicted by linear stability analysis, the first bifurcation occurs at $Ra_c = 5708$ and is marked by the onset of 2D corotating rolls. A second bifurcation takes place at $Ra = 9980$ leading to a 3D steady flow. Above $Ra = 11\,270$, the flow becomes oscillating. Beyond $Ra = 12\,100$, competition between a period-doubling cascade and an Eckhaus-like instability in the vertical direction is observed. The Eckhaus-like instability rapidly becomes dominant and leads to a temporally chaotic regime. Although the small spanwise extent of the configuration hampered the development of low-wave-number instabilities in that direction, it was nonetheless found that transverse effects characterized the development of instabilities and transition to chaos.

This was confirmed by the recent study of Cimarelli and Angeli [28], in which the flow pattern of natural convection between two differentially heated, infinite, vertical plates was investigated using DNS. Two different domain sizes were considered. In the larger domain, the 2D steady flow consisting of corotating rolls is observed from $Ra = 5800$ up to $Ra \approx 10\,200$ where a second bifurcation occurs and rapidly leads to flow to a fully chaotic regime. On the other hand, when Rayleigh number is decreased from the chaotic regime to the laminar regime, a hysteresis phenomenon was observed. In a smaller domain with reduced spanwise length, the second bifurcation at $Ra = 10\,200$ leads to a unsteady 2D pattern up to $Ra = 14\,000$, where 3D structure appears. We note that this last observation is different from the results found in [27] for a channel of smaller spanwise extent. In addition, Cimarelli and Angeli [28] found that finite amplitude disturbances led to a second bifurcation at $Ra = 10\,200$ towards a 3D steady flow pattern while infinitesimal disturbances give rise to an unsteady 2D pattern. If Ra is further increased, the simulation with finite disturbances recovers the 3D unsteady structure regime of the simulation with infinitesimal disturbances at $Ra = 14\,000$. They conclude that the flow regimes are extremely sensitive to the domain size, grid resolution, and perturbation amplitude. This makes the prediction of nonlinear simulation results quite difficult for a given set of parameters (Rayleigh number, plate aspect ratio).

Given the limitations of both linear stability analysis and nonlinear simulation, the motivation for the present paper is to combine the two approaches to investigate three-dimensional effects in the transition to chaos of natural convection. We first use a fast linear approach based on the Arnoldi method to determine the critical spanwise wave numbers characterizing the secondary instability. This has not been done in [27,28]. In particular, we investigate the sensitivity of the secondary instability with respect to a small deviation of vertical aspect ratio of the chosen domain by considering two different periodic lengths in the vertical direction. We note that the Arnoldi method's base flow is 2D, so that the eigenmodes are not constrained to be pure Fourier in the vertical direction, unlike earlier stability studies, but corresponds to combinations of them, which allows more flexibility in the definition of eigenmodes. The flow reconstructed from the most unstable linear eigenmodes is then compared to that obtained by nonlinear simulation when the Rayleigh number is slightly above the secondary stability threshold. Finally, the route to chaos is explored with nonlinear simulation using periodic plate aspect ratios which are close to the critical wavelengths provided by linear stability analysis.

II. PHYSICAL PROBLEM AND NUMERICAL APPROACHES

We consider the three-dimensional flow of air between two infinite vertical plates maintained at different temperatures. The configuration is represented in Fig. 1. The distance between the two plates is D , and the periodic height and depth of the plates are L_z and L_y , respectively. The temperature difference between the two plates is ΔT . The direction x is normal to the plates, the transverse direction is y , and the gravity g is opposite to the vertical direction z .

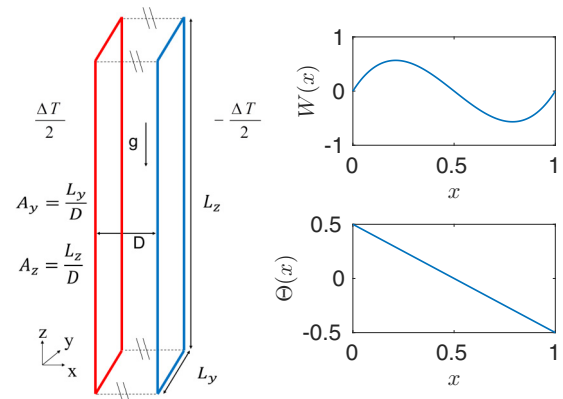


FIG. 1. Left: Configuration. Air flow ($Pr = 0.71$) between two vertical plates separated by a distance D and maintained at different temperatures: the hot plate (left, in red) is at temperature $\frac{\Delta T}{2}$ while the cold plate (right, in blue) is at temperature $-\frac{\Delta T}{2}$. Periodic boundary conditions are imposed in the vertical and in the spanwise direction. The periodic height and width of the plates are, respectively, L_z and L_y , and the corresponding aspect ratios are $A_y = L_y/D$ and $A_z = L_z/D$. The gravity g is opposite to the vertical direction z . Right: Steady laminar conduction solution profiles for the vertical velocity $W(x)$ and temperature $\Theta(x)$.

The fluid properties of air, such as the kinetic viscosity ν , thermal diffusivity κ , and thermal expansion coefficient β , are supposed to be constant. The four nondimensional parameters characterizing the flow are the Prandtl number $\text{Pr} = \frac{\nu}{\kappa}$, the Rayleigh number based on the width of the gap between the two plates $\text{Ra} = \frac{g\beta\Delta T D^3}{\nu\kappa}$, and the transverse and vertical aspect ratios $A_y = L_y/D$ and $A_z = L_z/D$, respectively. The Prandtl number of air is fixed to 0.71.

The flow is governed by the Navier-Stokes equations within the Boussinesq approximation. Here t denotes time, $\vec{u} = (u, v, w)$ is the velocity vector, p is the pressure, and θ is the temperature. D , ΔT , and $\kappa\sqrt{\text{Ra}}/D$ are chosen as references for length, temperature, and velocity, respectively. We note that the velocity scale corresponds to the velocity scaling expected in the laminar boundary layer of a vertical natural convection plate, which comes from balancing buoyancy and diffusion in the vertical momentum equation and balancing convection and diffusion in the temperature equation (see [29] for a full derivation).

The nondimensionalized equations are

$$\nabla \cdot \vec{u} = 0, \quad (1)$$

$$\frac{\partial \vec{u}}{\partial t} + \vec{u} \cdot \nabla \vec{u} = -\nabla p + \frac{\text{Pr}}{\sqrt{\text{Ra}}} \Delta \vec{u} + \text{Pr} \theta \vec{z}, \quad (2)$$

$$\frac{\partial \theta}{\partial t} + \vec{u} \cdot \nabla \theta = \frac{1}{\sqrt{\text{Ra}}} \Delta \theta \quad (3)$$

with Dirichlet boundary conditions at the plates,

$$\begin{aligned} \vec{u}(0, y, z, t) = \vec{u}(1, y, z, t) = 0, \quad \theta(0, y, z, t) = 0.5, \\ \theta(1, y, z, t) = -0.5, \end{aligned} \quad (4)$$

and periodic conditions in the y and z directions.

Equations (1)–(4) admit an $O(2) \times O(2)$ symmetry. One $O(2)$ symmetry corresponds to the translation in the transverse direction y and the reflection $y \rightarrow -y$, while the other corresponds to the translations in the vertical direction z and a reflection that combines centrosymmetry and Boussinesq symmetry: $(x, z, T) \rightarrow (1-x, -z, -T)$.

The equations of motion (1)–(4) admit an analytic steady solution (U, V, W, Θ) , the pure conduction state, which depends only on the x direction and constitutes the base flow:

$$\begin{aligned} U = 0, \quad V = 0, \quad W(x) = \frac{1}{6}\sqrt{\text{Ra}}\left[\left(x - \frac{1}{2}\right)^3 - \frac{1}{4}\left(x - \frac{1}{2}\right)\right], \\ \times \Theta(x) = -\left(x - \frac{1}{2}\right). \end{aligned} \quad (5)$$

The velocity and temperature profiles corresponding to the steady conduction solution are represented in Fig. 1 (right). The derivation of linearized 3D Navier-Stokes equations and a description of the Arnoldi-based linear stability analysis approach are given in the Appendix. Both the fully nonlinear and linearized equations are integrated in the current study with spectral codes [30–32]. The Chebyshev-Fourier collocation method is used for the spatial discretization. Incompressibility is enforced by the projection-correction method. The equations are integrated in time with a second-order mixed explicit-implicit scheme. We established spatial convergence of the flow resolution.

The cost of integration of the linearized 3D Navier-Stokes equations [Eq. (A1) in the Appendix] for one typical configuration is about several hours. With the Arnoldi method, it reduces to only tens of minutes for the same configuration on an ordinary personal computer. In contrast, integration in time of the full 3D nonlinear Navier-Stokes equation (1)–(4) requires several hundred hours for a single configuration to reach its asymptotic state on the IBM Intel-based cluster of the French Institute for Development and Resources in Intensive Scientific Computing (IDRIS).

III. LINEAR STABILITY ANALYSIS

The onset of the secondary instability leads the 2D flow to a 3D steady state as established in the literature [23–25]. In this section, we determine the critical spanwise wave number associated with the roll size given by the periodic length of the plate in the vertical direction, and the flow patterns associated with the corresponding instabilities.

A. Base flow

Both linear stability analysis and nonlinear integration confirm that the first instability occurs at $\text{Ra}_{c1} = 5708$ and is characterized by the appearance of 2D corotating rolls [23–25,27] with a critical wave number $k_{zc} = 2.81$. As mentioned in [27], the vertical translation invariance is replaced with a D_4 symmetry, and the centrosymmetry due to the Boussinesq approximation is conserved.

To represent the flow structures, shown in Fig. 2, we use the Q criterion devised in [33] to visualize coherent structures in turbulent flows. The Q criterion is defined as $Q = \frac{1}{2}(\Omega_k \Omega_k - E_{ij} E_{ij})$, where Ω_k is the vorticity $\Omega_k = \frac{1}{2}(\frac{\partial u_i}{\partial x_j} - \frac{\partial u_j}{\partial x_i})$ and E_{ij} is the rate of strain tensor $E_{ij} = \frac{1}{2}(\frac{\partial u_i}{\partial x_j} + \frac{\partial u_j}{\partial x_i})$. Values of Q therefore represents a measure of the local balance between

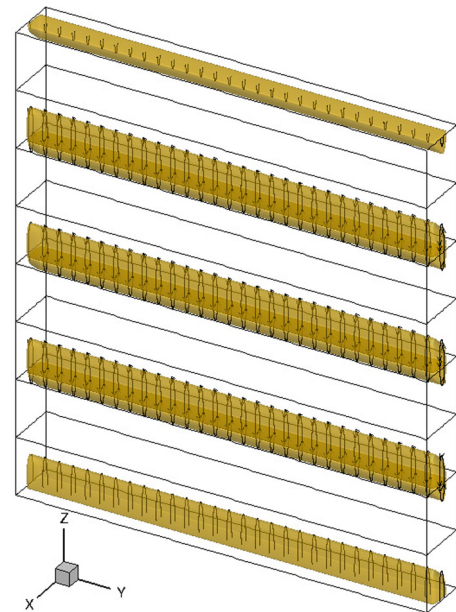


FIG. 2. Rolls visualized with the Q criterion using an isovalue of $Q = 0.1$ at $\text{Ra} = 6050$, $t = 2000$, and $A_z = 9$.

the vorticity magnitude and the strain rate. A positive value of Q provides an indication of strong vortical structures.

B. Methodology

We use the Arnoldi method to determine the critical Rayleigh number Ra_{c2} at which secondary instability in the spanwise direction y first occurs, and the corresponding eigenmodes. For a given vertical aspect ratio A_z , we wish to determine the critical Rayleigh number Ra_{c2} at which the secondary instability occurs and the corresponding spanwise critical wave number k_{yc} . At a given wave number k_{yi} , the code is run for different Ra_j . Each run yields several leading eigenvalues. The real part of the first leading eigenvalue σ_{ij} determines the stability of the mode k_{yi} at Ra_j . As σ_{ij} increases almost linearly with Ra_j , linear extrapolation can be used to find the critical Rayleigh number Ra_{c2i} . Then the procedure is repeated for a range of k_{yi} to calculate the corresponding Ra_{c2i} . The neutral curve can be obtained by plotting Ra_{c2i} as a function of k_{yi} . The minimum of the neutral curve corresponds to Ra_{c2} .

The vertical ratio A_z should be large enough to allow interaction between the structures (i.e., low-wave-number instabilities). We also wish to study the sensitivity of the secondary instability to the roll size, i.e., the exact value of k_z . Since $k_{zc} = 2.81$, where k_{zc} is the critical wave number of the primary instability, we chose to study the cases $A_z = L_z/D = 9$ and $L_z/D = 10$, which both accommodate four rolls.

C. Case $A_z = 9$ ($k_z = 2.79$)

For the case $A_z = 9$, the wave number associated with the primary instability (2D rolls) is $k_z = 2.79$, which is very close to the critical wave number $k_{zc} = 2.81$. Ra_{c2} is found to be 6056, and $k_{yc} = 1.6$ (see the neutral curve in Fig. 3), and σ is real so the most unstable mode is stationary. This agrees well with previous results [23,24]. The value of k_{yc} appears to correspond to that associated with monotone instability A.

The different components of the most unstable eigenmode (velocity components in u , v , and w and temperature θ) are represented on the vertical center plane $x = 0.5$

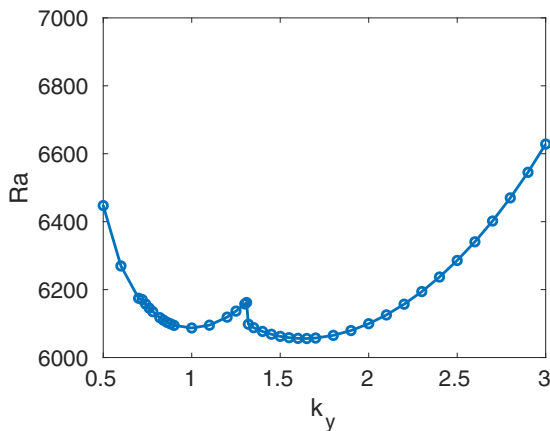


FIG. 3. Neutral curve, $\sigma(Ra_{c2i}) = 0$, as a function of the wave number k_y , $A_z = 9$

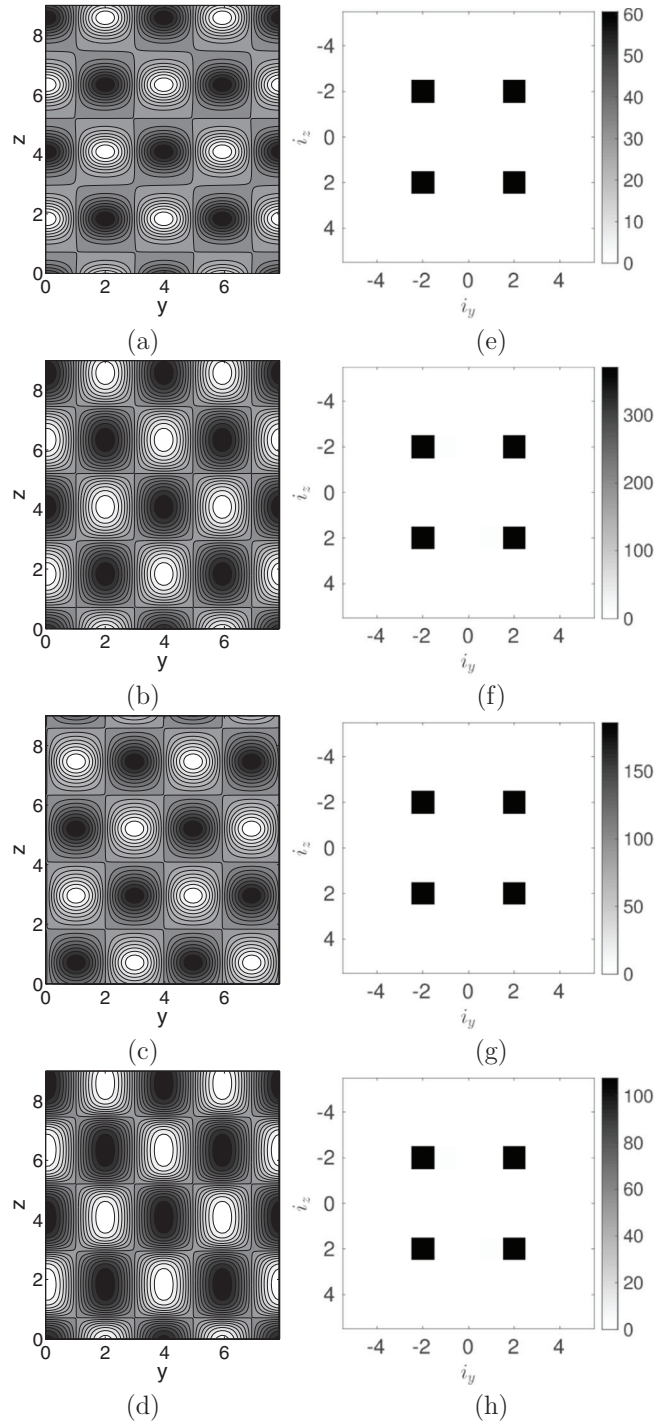


FIG. 4. Arnoldi eigenmode at $Ra = 6100$ with $A_z = 9$ on the central plane $x = 0.5$. Left, from top to bottom: (a–d) Velocity components u , v , and w and temperature θ . Right, from top to bottom: Fourier modulus $|\hat{u}(i_y, i_z)|$, $|\hat{v}(i_y, i_z)|$, $|\hat{w}(i_y, i_z)|$, and $|\hat{\theta}(i_y, i_z)|$.

Figs. 4(a)–4(d). We checked that similar remarks to those made below would hold for any other vertical plane $x = \text{const}$.

Examination of the Fourier spectra allows direct identification of the characteristic wavelengths of a given solution. The Fourier transform of the eigenmode in the directions y and z was therefore computed. Due to the periodic directions, any

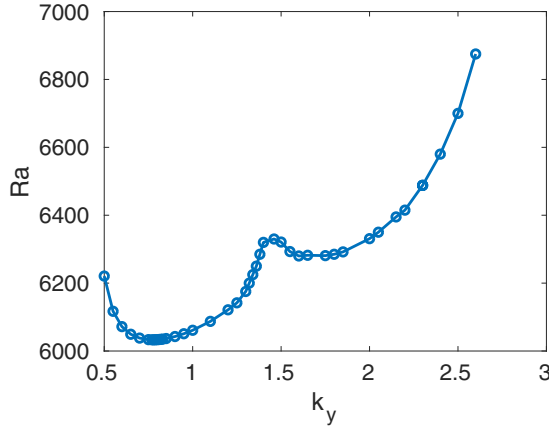


FIG. 5. Neutral curve, $\sigma(Ra_{c2}) = 0$, as a function of the wave number k_y , $A_z = 10$.

physical quantity $q = (u, v, w, \theta)$ can be represented as

$$q(x, y, z) = \sum_{i_y} \sum_{i_z} \hat{q}_x(i_y, i_z) \exp\left(\frac{2i\pi i_z z}{L_z}\right) \exp\left(\frac{2i\pi i_y y}{L_y}\right)$$

where i_y and i_z are horizontal wave numbers. In the rest of the paper we drop the subscript x and will note $\hat{q}(i_y, i_z)$ for $\hat{q}_x(i_y, i_z)$. By construction, each eigenmode of the Arnoldi method corresponds to a single value of $|i_y|$. The modulus of the most unstable eigenmode components $|\hat{q}(i_y, i_z)|$ is represented in Figs. 4(e)–4(g). We see that the modes associated with the pattern are all characterized by $|i_y| = |i_z| = 2$. This regular flow pattern corresponds to the mode A which was identified in [23,24] and corresponds to local roll pairing.

D. Case $A_z = 10$ ($k_z = 2.51$)

For the case $A_z = 10$, we have $k_z = 2.51$. The neutral curve is shown in Fig. 5. The critical Rayleigh number is found to be $Ra_{c2} = 6033$, and the critical spanwise wave number k_{yc} is equal to 0.78. This also corresponds to a stationary mode, and the value of the wave number is consistent with the monotone instability B of Chait and Korpela [24].

The flow pattern associated with the unstable eigenmode is represented in Fig. 6 for the central plane $x = 0.5$ along with the corresponding spatial spectra. All components of the eigenmode (velocity components u , v , and w and temperature θ) are represented. Unlike the previous case (mode A), different dominant wavelengths characterize the different flow components: the vertical velocity w and the temperature θ are dominated by a mode $i_z = 5$, while the horizontal components u and v are characterized by a lower wave number $i_z = 1$.

This is consistent with the analysis of Chait and Korpela [24]. However, although there is a strong similarity between this mode and the B instability of Chait and Korpela, it is not entirely clear that our mode exactly corresponds to mode B since, as mentioned earlier, Chait and Korpela’s study only admits pure Fourier modes in the vertical direction. We will therefore denote this mode C to avoid ambiguity.

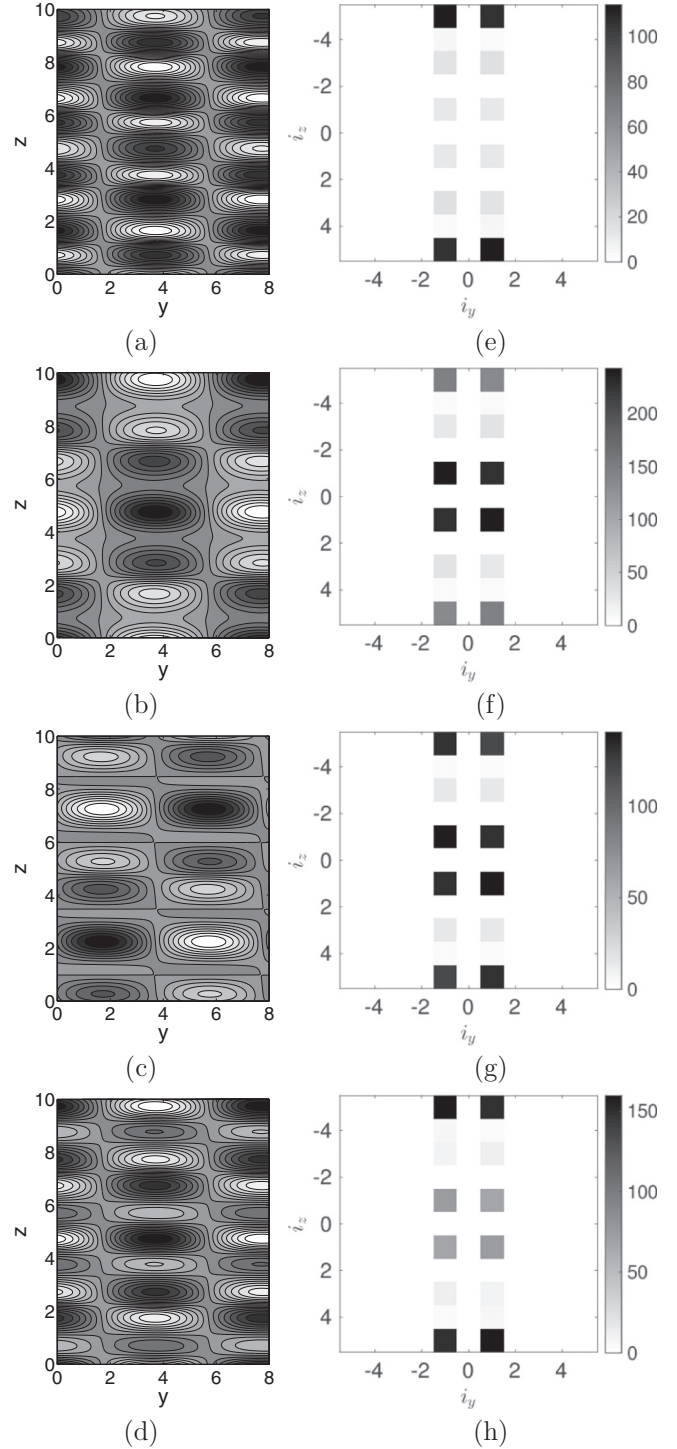


FIG. 6. Arnoldi eigenmode at $Ra = 6050$ with $A_z = 10$ on the central plane $x = 0.5$. Left, from top to bottom: (a–d) Velocity components u , v , and w and temperature θ . Right, from top to bottom: Fourier modulus $|\hat{u}(i_y, i_z)|$, $|\hat{v}(i_y, i_z)|$, $|\hat{w}(i_y, i_z)|$, and $|\hat{\theta}(i_y, i_z)|$.

E. Comparison and discussion

Comparison of Figs. 3 and 5 shows the presence in both cases of two similar lobes with two local minima around $k_y \sim 1.6$ and 0.8. Each minimum appears to correspond to a different instability mechanism. The minimal Rayleigh values associated with each lobe are close for $A_z = 9$ ($k_z = 2.8$) but

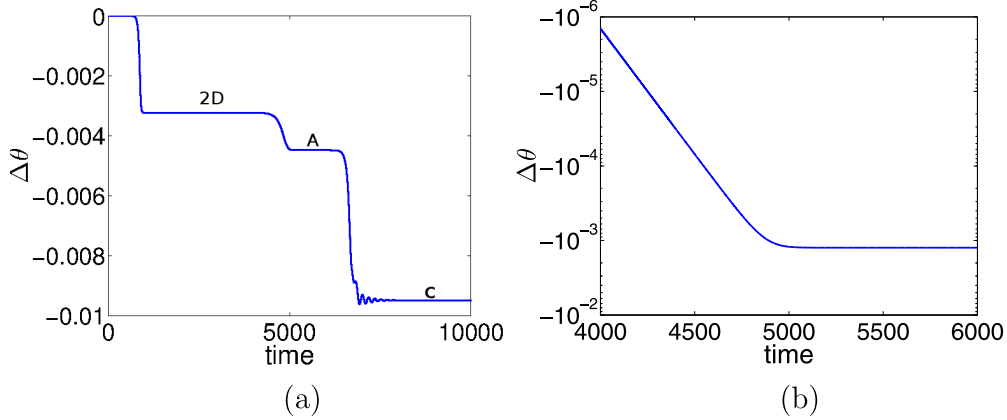


FIG. 7. (a) Time series of temperature at point (0.0381, 0.122, 4.96) in the boundary layer near the hot wall at $Ra = 6100$, $A_z = 9$. (b) An enlargement of (a) for $4000 < t < 6000$ on a logarithmic scale.

the absolute minimum (critical Rayleigh number) is associated with the higher wave number, while it corresponds to the lower wave number in the case $A_z = 10$ ($k_z = 2.5$). We checked that these different results were consistent with the straightforward integration of the linearized equations.

The nature of the most unstable mechanism is therefore quite sensitive to the exact value of the wave numbers allowed in both the vertical and transverse directions. Moreover, since the growth rate of each instability is relatively close, competition between the different mechanisms is likely to take place. This will be examined in more detail using nonlinear simulation in the next section for $A_y = 8$. Linear stability analysis shows that this spanwise periodic length can accommodate twice the pattern A ($k_y \sim 1.6$) or once the pattern C ($k_y \sim 0.8$) in the spanwise direction.

IV. COMPARISON WITH 3D NONLINEAR SIMULATION FOR $A_y = 8$

In this section, we integrate the nonlinear Navier-Stokes equations (1)–(4) and follow the various bifurcation branches, starting from the fixed point corresponding to the 2D base flow.

A. $A_z = 9$

The time series of the temperature perturbation $\Delta\theta$, defined as the difference between the temperature field of the flow θ and that of the base flow Θ ($\Delta\theta = \theta - \Theta$), is computed at the location (0.0381, 0.122, 4.96), located close to the hot plate, and represented in Fig. 7.

Three different steady or quasisteady states can be identified. A plateau corresponding to 2D rolls is observed at first, then the flow becomes three-dimensional as can be seen in Fig. 8.

1. Transient 3D pattern associated with instability A: Wavy rolls

A blow-up of the temperature signal for the times $4000 < t < 6000$ is represented in logarithmic scale in Fig. 7(b). The amplitude of temperature disturbance grows exponentially for $4000 < t < 4500$, in agreement with linear stability theory, then increases at a lower rate for $t > 4700$ before settling to a steady value (saturation). As shown by [27,34,35], the temporal evolution of the amplitude provides information about the local

normal form in the neighborhood of the bifurcation and therefore can help determine its nature (supercritical or subcritical). Here examination of the amplitude shows that the coefficient of the cubic term in the normal form of the pitchfork bifurcation is negative, therefore this bifurcation is supercritical. We note that it is also a circle bifurcation owing to the invariance of the equations with respect to transverse translations.

The DNS results confirm the linear stability predictions that the most unstable spanwise mode is $k_y = 1.6$. The flow structure consists of four steady corotating rolls with a wavy distortion in the transverse direction. As can be seen in Fig. 8, at the location of a crest, the streamlines escape from a roll to join the adjacent roll above it. This connection between the rolls is somewhat similar to the vortex pairing observed in the mixing layer [36], which is also a subharmonic instability. Note that there is no break in the Q contour, which means that the local vorticity remains larger than the rate of strain.

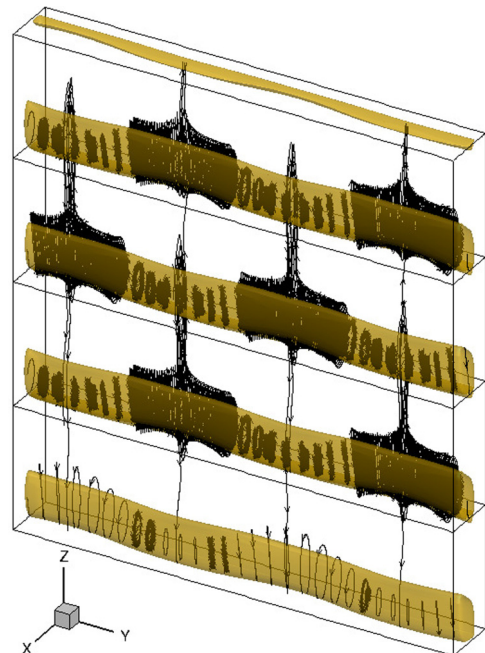


FIG. 8. Isosurface of Q criterion $Q = 0.1$ and streamlines, at $t = 6000$, $Ra = 6100$, $A_z = 9$.

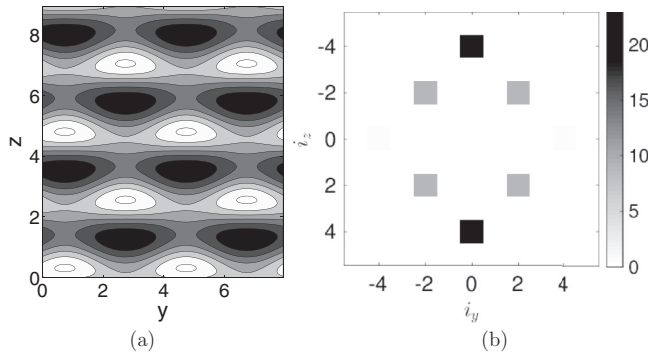


FIG. 9. (a) Temperature contour on the vertical plane $x = 0.0381$. (b) Corresponding 2D spatial spectrum $|\hat{\theta}(i_y, i_z)|$ ($i_y, i_z = -5, 5$) for the fluctuations, $t = 6000$, $Ra = 6100$, $A_z = 9$.

The temperature contour on the vertical plane $x = 0.0381$ is represented in Fig. 9(a). The corresponding spatial spectrum is shown in Fig. 9(b). It can be seen that $\hat{\theta}(0, 4)$ and $\hat{\theta}(2, 2)$, which, respectively, represent the 2D rolls and the wavy distortion, are the principal modes constituting the pattern.

2. Steady 3D pattern associated with instability B

As can be seen in Fig. 7(a), the temperature perturbation with respect to the base flow shifts from the second plateau, associated with the monotone instability A, to a third plateau, associated with the monotone instability B, at $t \sim 7000$. Using the normal-form analysis described above, the local oscillation of time series in Fig. 7(a) at $t \sim 7000$ indicates that the instability is subcritical, since the overshoot of the oscillation following the period of exponential growth shows that the coefficient of the cubic term in the normal form of a bifurcation is positive (see [34,35]). The final flow pattern is shown in Fig. 10. Although remains of pattern A

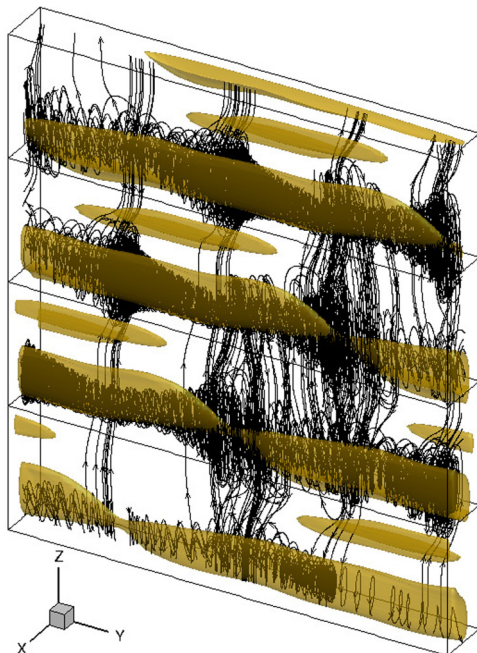


FIG. 10. Isosurface of Q criterion $Q = 0.1$ and streamlines for the flow pattern at $t = 9000$, $Ra = 6100$, $A_z = 9$.

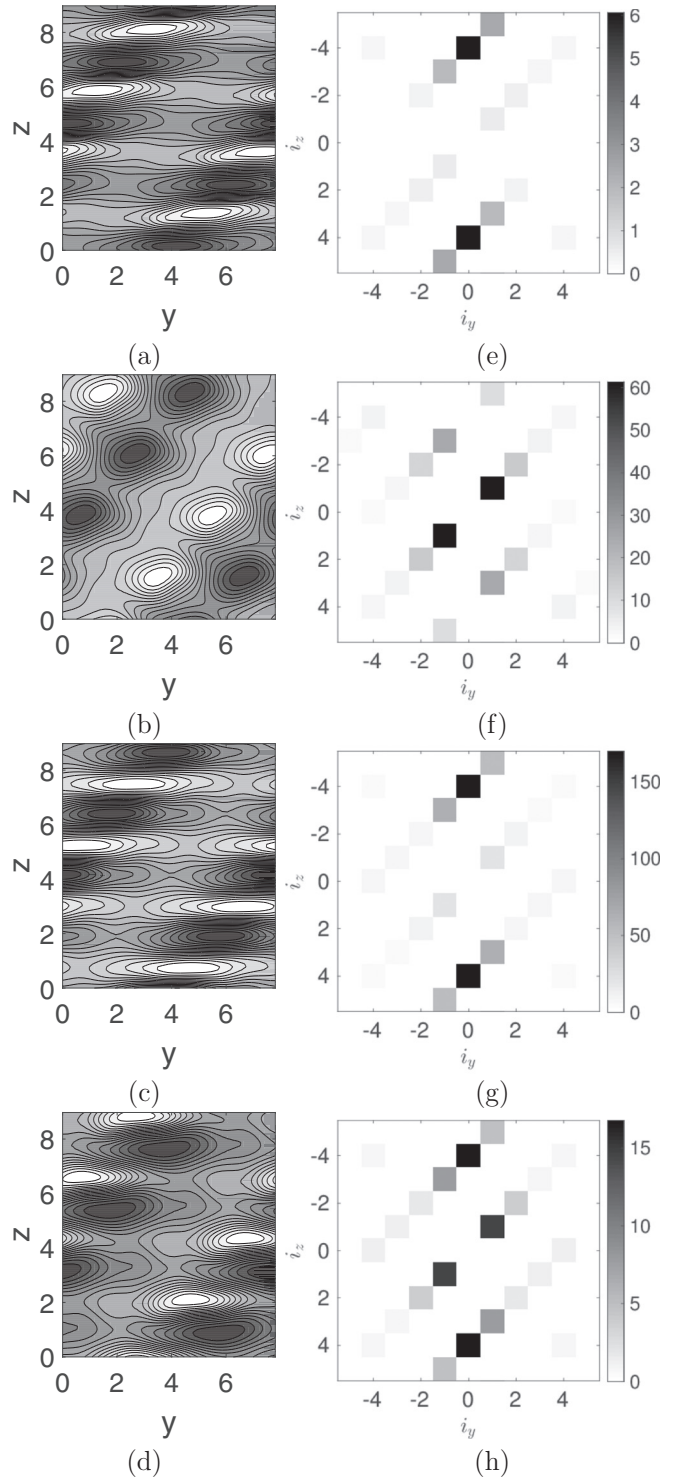


FIG. 11. Left: Flow pattern on plane $x = 0.0381$ at $t = 10000$ and $Ra = 6100$ with $A_z = 9$. (a-c) Velocity components u , v , and w . (d) Temperature θ isocontours. Right, from top to bottom: Fourier coefficients (e) $|\hat{u}(i_y, i_z)|$, (f) $|\hat{v}(i_y, i_z)|$, (g) $|\hat{w}(i_y, i_z)|$, and (h) $|\hat{\theta}(i_y, i_z)|$.

are still present, the dominant feature of the flow consists of transverse rolls with streamline excursions over a single, limited portion of its spanwise extent—which we will call the defect. The defects form an oblique line in the (x, z) plane. The orientation of the line can be either from the top-right

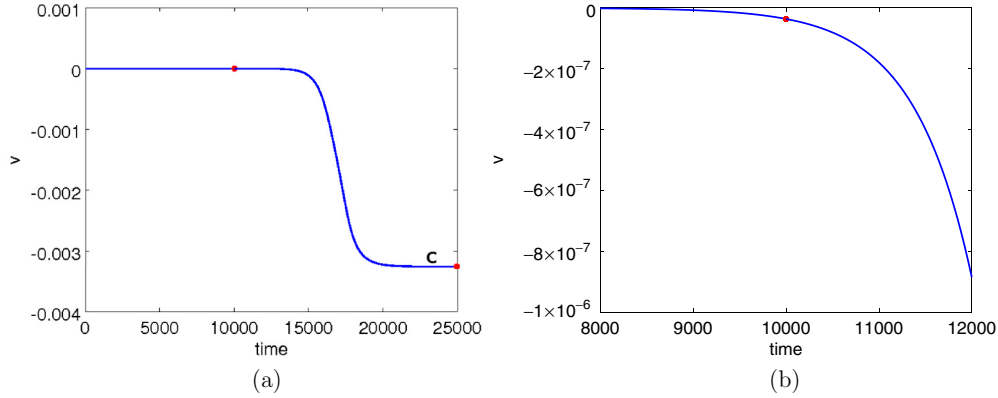


FIG. 12. (a): Time series of spanwise velocity v at point $(0.0381, 0.585, 6.985)$ at $Ra = 6050$, $A_z = 10$. (b) Enlargement of (a) for $8000 < t < 12000$. The red dots correspond to the instantaneous fields at times $t = 10000$ and 25000 shown, respectively, in Figs. 13 and 14.

to the bottom-left or from the top-left to the bottom right, since the system (1)–(4) is invariant under a reflection with respect to any plane perpendicular to the plates ($y = \text{const}$). Note that at the location of the defect a strong decrease is observed in the value of Q , which corresponds to a relative increase in the local rate of strain, associated with roll thinning and possible breaking. We also note the presence of secondary vortical structures between the main rolls, suggesting the presence of nonlinear interactions.

The velocity and temperature fields at $t = 10000$ on the vertical plane close to the hot plate ($x = 0.0381$) are represented in Figs. 11(a)–11(d). The corresponding 2D spatial spectra shown in Figs. 11(e)–11(h) confirm that the principal modes associated with the pattern are $\hat{\theta}(0,4)$ (2D rolls) and $\hat{\theta}(1,-1)$ (mode C). We note that, since Eqs. (1)–(4) are invariant by reflection with respect to any vertical plane $y = \text{const}$, the modes $\hat{\theta}(1,-1)$ and $\hat{\theta}(1,1)$ are equivalent solutions. The modes $\hat{\theta}(\pm 2, \pm 2)$ are also present with slightly different amplitudes, which confirms the coexistence of the two instability mechanisms.

Although the Rayleigh number of the configuration is very close to the critical Rayleigh of instability A, it seems that mode A is in fact unstable to a low-wave-number instability (similar to C). To check this, we integrated the nonlinear equations at $Ra = 6060$ —close to the critical Rayleigh number $Ra_{c2} = 6056$ —from an initial condition containing exclusively the pattern A observed at $Ra = 6100$. We found that the flow also converged towards a steady state consisting of a mixture of modes A and C. This hysteresis phenomenon suggests that the pattern A predicted by the linear stability analysis is subcritically unstable to a low-wave-number instability. We therefore suspect the presence of a cusp bifurcation involving three equilibria: the straight (2D) rolls, the wavy rolls (higher-wave-number instability A), and the thinning rolls (low-wave-number instability C).

B. $A_z = 10$

As in the case above, the fully nonlinear Navier-Stokes equations are integrated in time at $Ra = 6050$ starting from the base flow consisting of 2D rolls. The temporal evolution of the spanwise velocity v at the point $(0.0381, 0.585, 6.985)$, located close to the hot plate, is represented in Fig. 12, and

shows that the flow reaches a steady state around $t \sim 20000$. To study how the flow reaches its asymptotic state, we selected the instant $t = 10000$ (materialized by a red dot in Fig. 12), which corresponds to a moment where the perturbations grow exponentially, as can be seen in Fig. 12(b), and represented in Fig. 13 the difference between the instantaneous flow and the 2D base flow. We see that the perturbation corresponds to the most unstable eigenmode predicted by linear stability analysis, i.e., mode C.

The pattern is very similar to the eigenmode displayed in Fig. 6 except for the fact that a particular direction is selected—the phase of the unstable mode is not imposed in the nonlinear simulation, while a zero phase is imposed in the Arnoldi calculation. The 2D spatial spectrum of the perturbation, shown in the right column of Fig. 13, confirms that the most energetic modes are $\Delta\hat{\theta}(1,1)$ and $\Delta\hat{\theta}(1,5)$, which is consistent with the linear stability prediction of mode C.

The final flow pattern at $t = 25000$ is shown in Fig. 14 for a vertical plane. As can be seen, this steady state is characterized by localized thinning of rolls (defects) along an oblique direction. Examination of the spectra in Fig. 14 confirms that the mode $i_y = 1$ is present. However, the mode $(\pm 2, \pm 2)$ is also noticeable, particularly in the spanwise component v and the vertical component w . We note that the Fourier mode $(i_y, i_z) = (0,0)$ corresponding to the spatial average has been omitted from the spectrum. It is not clear whether these modes appear through nonlinear interaction of the modes associated with instability C, or arise through a linear instability of type A. We note that the modes characterizing the temperature pattern for $A_z = 10$ (last row of Fig. 14) are the same as in the case $A_z = 9$ (Fig. 11), but with different amplitudes. More modes appear to be excited in the latter case, suggesting stronger nonlinear interactions.

V. NONLINEAR EVOLUTION AND SUBSEQUENT BIFURCATIONS OF THE FLOW FOR $A_y = 8$ and $A_z = 9$

A. Characteristics of the simulations

In this section, we use DNS to study the sequence of flow bifurcations leading to temporal chaos. Owing to the cost of such a simulation, only one configuration is studied. We choose $A_y = 8$ and $A_z = 9$, which has a large

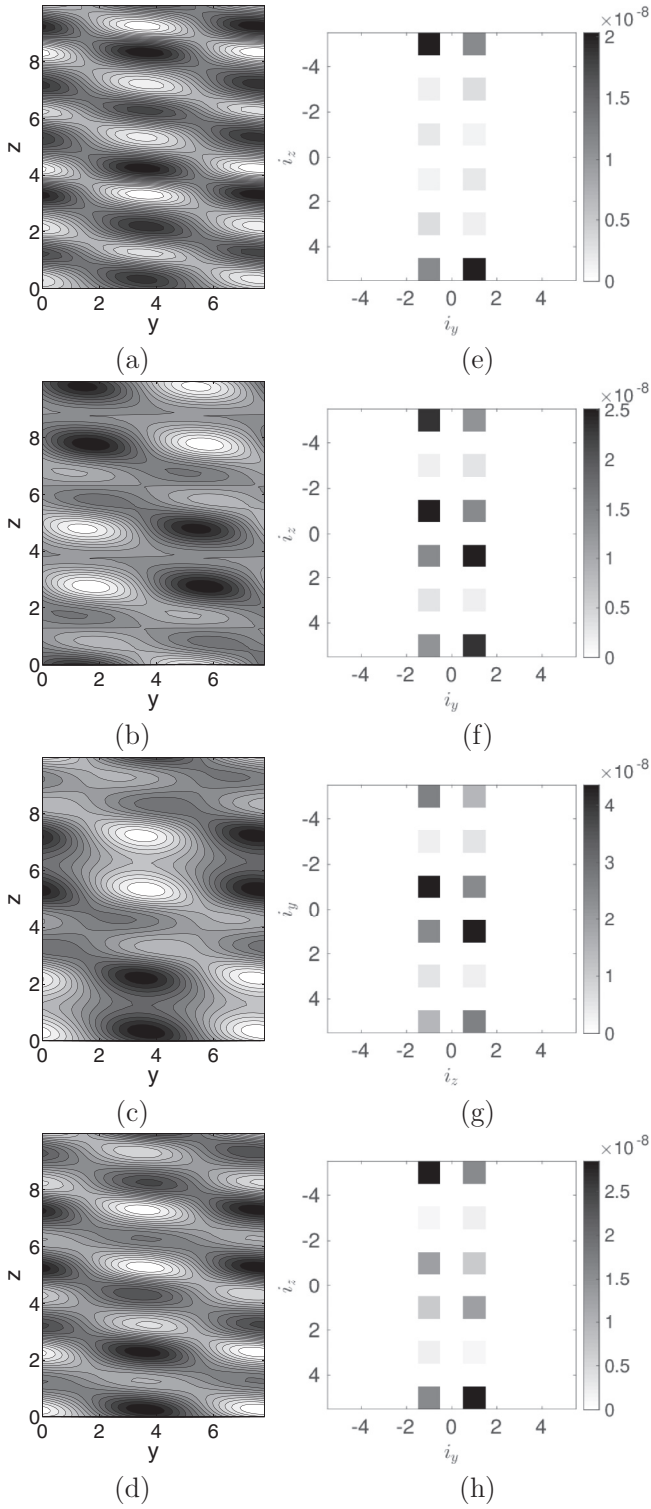


FIG. 13. Flow perturbation pattern on the central plane $x = 0.5$ at $t = 10000$ and $Ra = 6050$ with $A_z = 10$. Left: Velocity components ($\Delta u, v, \Delta w$) (a–c) and temperature (d) $\Delta\theta$ contours. Right, from top to bottom: Fourier coefficients (e) $|\Delta\hat{u}(i_y, i_z)|$, (f) $|\Delta\hat{v}(i_y, i_z)|$, (g) $|\Delta\hat{w}(i_y, i_z)|$, and (h) $|\Delta\hat{\theta}(i_y, i_z)|$.

enough spanwise dimension to accommodate both critical spanwise wavelengths. The initial condition is taken to be the steady conduction solution defined by Eq. (5). We used 40 and 160 Chebyshev modes for the spatial discretizations

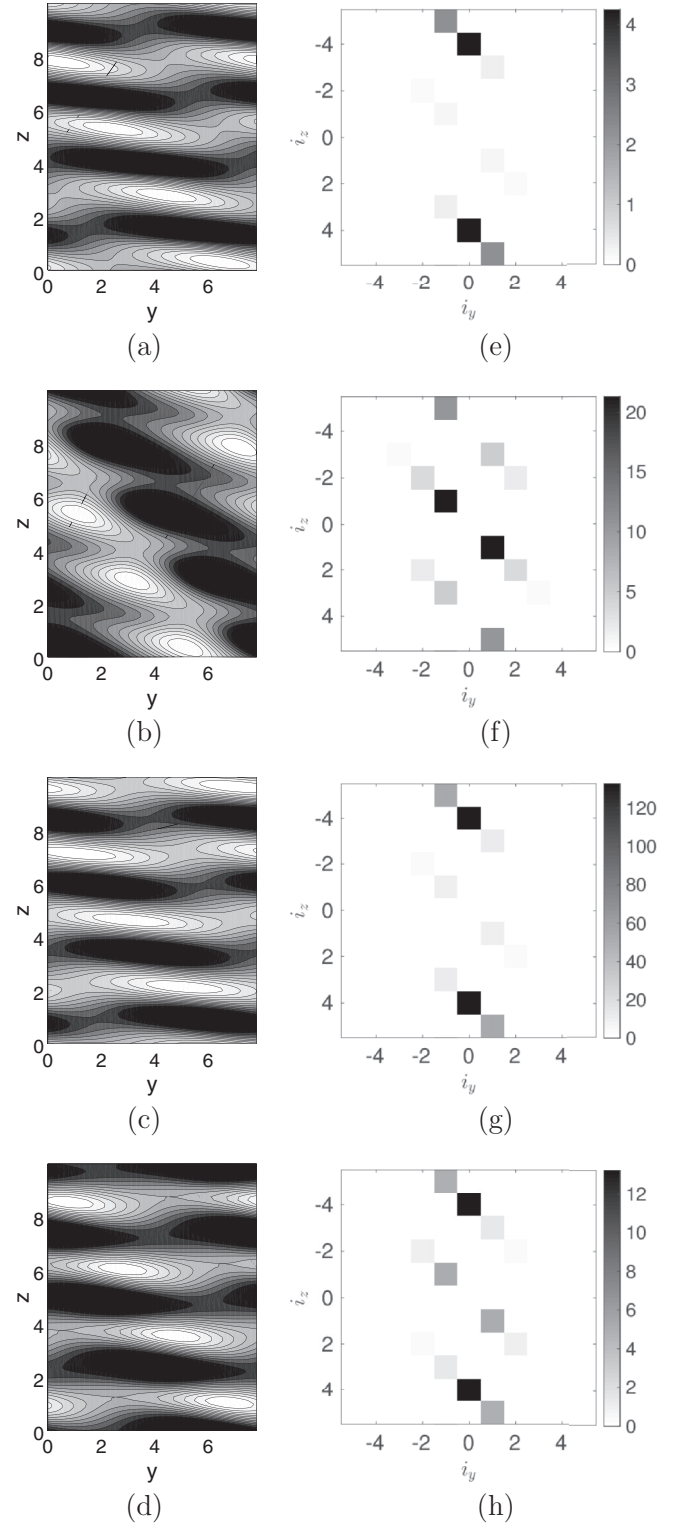


FIG. 14. Flow field on the central plane $x = 0.5$ at $t = 25000$ and $Ra = 6050$ with $A_z = 10$. Left: Velocity components u, v, w (a–c) and temperature (d) θ contours. Right, from top to bottom: Fourier modulus $|\hat{u}(i_y, i_z)|$, $|\hat{v}(i_y, i_z)|$, $|\hat{w}(i_y, i_z)|$, and $|\hat{\theta}(i_y, i_z)|$.

in the directions x and z , respectively, and 130 Fourier modes for the y direction. Calculations were carried out at $Ra = 6050, 6070, 6080, 6100, 6150, 6180, 6200, 6250$, and

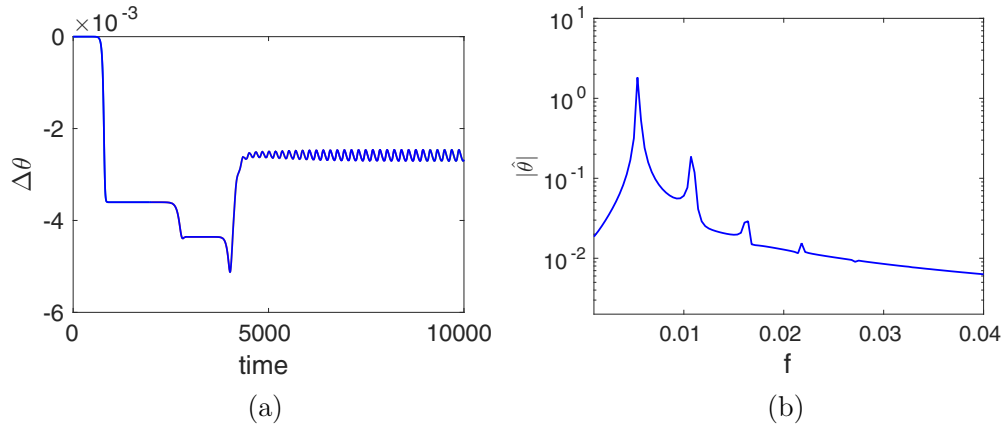


FIG. 15. (a) Time series of temperature at the point (0.0381, 0.122, 4.96) in the boundary layer near the hot wall, $Ra = 6150$. (b) Temporal spectrum of the periodic portion $t \in [8000, 10\,000]$ of the signal (a).

6300. We only show results for the three cases $Ra = 6150, 6250$, and 6300 , which present distinctive features.

B. $6150 \leq Ra \leq 6200$: 3D oscillating flow

The 3D pattern becomes time dependent when Ra is increased to 6150. The temperature time series at the point (0.0381, 0.122, 4.96) in the hot boundary layer is plotted in Fig. 15(a). Figure 15(b) shows that it corresponds to a periodic signal of frequency $f_1^{Large} = 0.00536$, which is much lower than the value of $f_1 = 0.036$ found in [27] for a constrained configuration. Computations at $Ra = 6180$ and 6200 yielded similar values of the frequency, which supports the conjecture that this is a Hopf bifurcation.

Figure 16 represents the flow structures at two different instants. They consist of corotating rolls with a local defect, as can be seen in Fig. 16(a). In Fig. 16(b), the discontinuities of the Q isosurface disappear, which indicates that the defect region shrinks. The periodic oscillation is characterized by the growth and shrink of the defect associated with roll thinning and streamline excursions.

The temperature contours on the vertical plane $x = 0.0381$ are represented in Fig. 17 (left) at different instants. Local roll

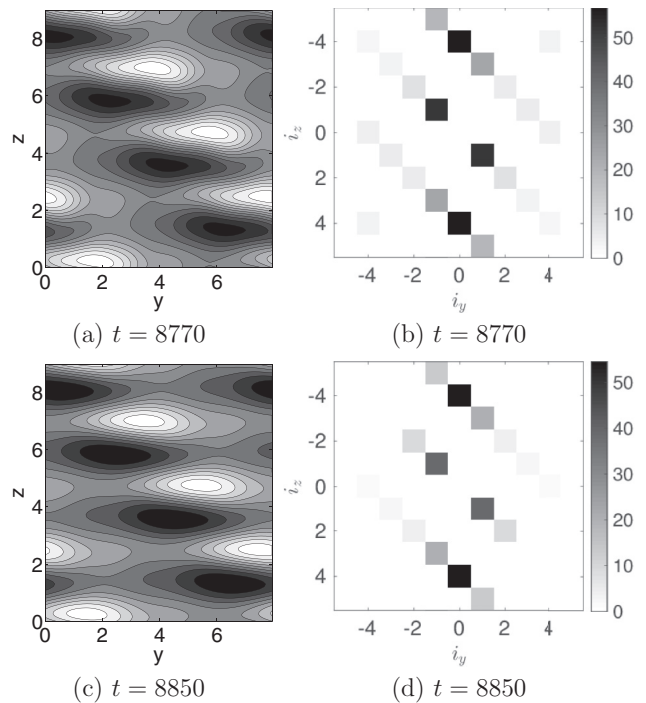


FIG. 17. Left column: The temperature contours on the vertical plane $x = 0.0381$. Right column: Corresponding spatial 2D Fourier modes $|\hat{\theta}(i_y, i_z)|$ ($i_y, i_z = -5, 5$) for the fluctuations, $Ra = 6150$.

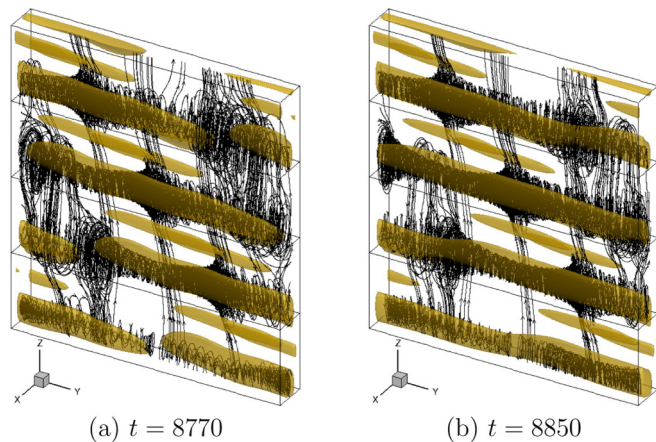


FIG. 16. Nonlinear simulation of flow structures at two different instants: isosurface of Q criterion $Q = 0.1$ and streamlines, $Ra = 6150, A_z = 9$.

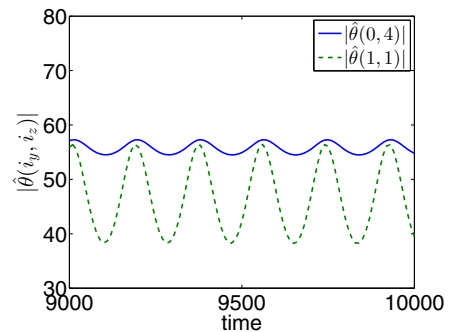


FIG. 18. Temporal evolution at $Ra = 6150$ of the spectral coefficients $|\hat{\theta}(i_y, i_z)|$ on the vertical plane $x = 0.0381$ (close to the hot plate) for the two most energetic modes.

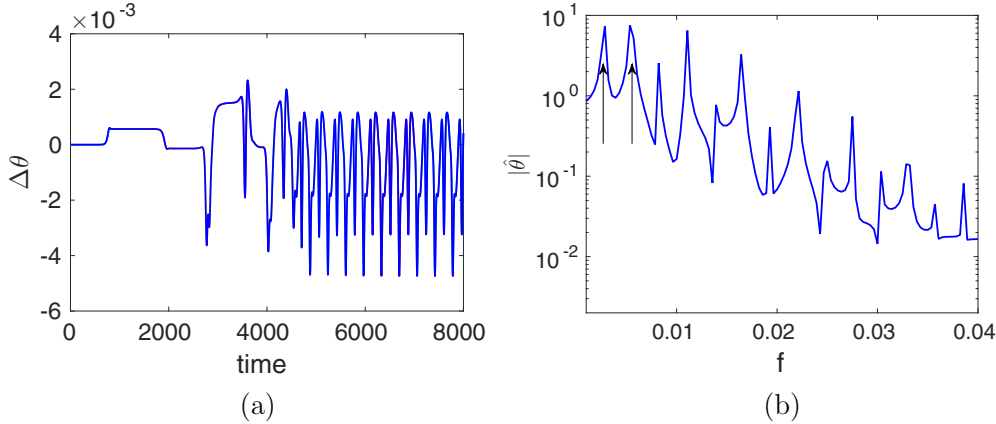


FIG. 19. (a) Time series at $Ra = 6250$ of the temperature perturbation at the point $(0.0381, 0.122, 4.96)$ in the hot boundary layer. (b) Temporal spectrum of the periodic portion of the signal represented in (a) for $t \in [5000, 8000]$.

thinning—defects—are noticeable, along with roll waviness, indicating that modes associated with both low-wave-number (C) and higher-wave-number (A) instabilities are present, as can be confirmed in Fig. 17 (right). Similarity with Fig. 11 is observed.

Figure 18 shows that the temporal evolution of the principal modes $\hat{\theta}(0,4)$ and $\hat{\theta}(1,1)$ is periodic and that the modes have the same phase. The amplitude of the mode $\hat{\theta}(0,4)$ corresponding to the primary rolls is almost constant, while the mode $\hat{\theta}(1,1)$ has a significant amplitude variation. These two modes capture 84.17% of the variance of the thermal fluctuations.

C. $Ra = 6250$: Period-doubling bifurcation

The temporal behavior of the flow is modified when Ra is further increased to $Ra = 6250$. The time series of the temperature perturbation at the point $(0.0381, 0.122, 4.96)$ is shown in Fig. 19(a). The temporal spectrum of the periodic portion $t \in [5000, 8000]$ in Fig. 19(b) shows that the largest amplitude is located at the frequency $f_1^{Large} = 0.00536$, which is identical to that found in Sec. VB at $Ra = 6150$, while the second largest amplitude corresponds to the frequency $f_{1/2}^{Large} = 0.00286 \sim f_1^{Large}/2$.

The topology of the flow again consists of rolls which are distorted in the transverse direction. The evolution of the flow structure during half an oscillation period (the whole oscillation period is twice as large as the previous case $Ra = 6150$) is represented in Fig. 20. At $t = 7600$ and 7780 , the flow patterns shown in Figs. 20(a) and 20(d) are similar and characterized by strong roll thinning and roll waviness. In contrast, roll distortion is weaker at $t = 7660$ and 7720 [Figs. 20(b) and 20(c)]. We note that the positions of the defects are shifted about half a wavelength $A_y/2$ in the y direction over half of the double-period cycle (they return to their original positions after another half cycle). We note that a similar behavior was found and studied in detail for a reduced domain consisting of a single roll [37].

The temperature on the vertical plane $x = 0.0381$ and its spatial spectrum are represented in Fig. 21 at selected times indicated in Fig. 20. The observations made above are confirmed: at $t = 7600$ and 7780 [Figs. 21(a) and 21(d)], the flow is

characterized by the excitation of many modes corresponding to instabilities A and C and nonlinear interactions.

The most energetic modes are $\hat{\theta}(0,4)$, $\hat{\theta}(2,2)$, and $\hat{\theta}(1,1)$ as well as the mode $\hat{\theta}(1,3)$. The latter could result from the interaction between the modes $\hat{\theta}(0,4)$ and $\hat{\theta}(1,1)$, but is also present to a smaller extent in the eigenmode associated with the low-wave-number instability C. In any case, nonlinear interactions are still limited: the three principal modes and the

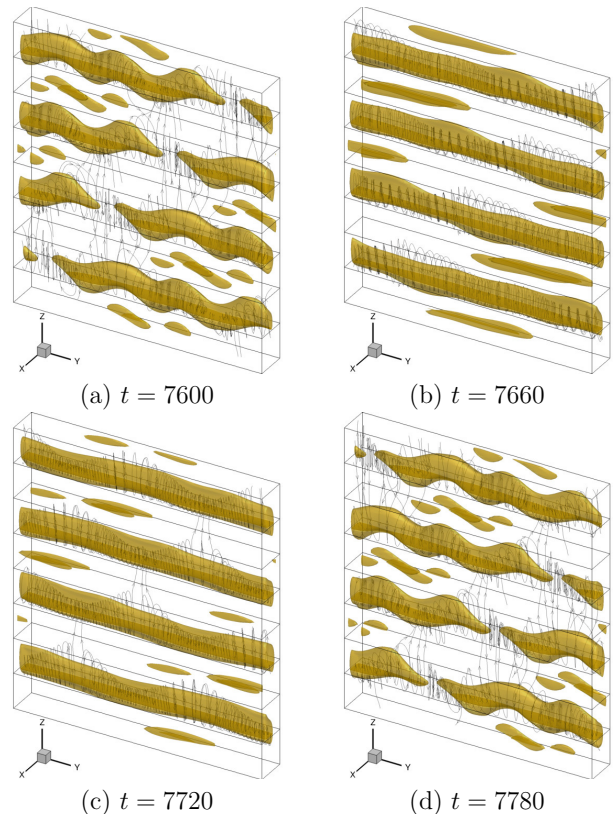


FIG. 20. Flow structures $Ra = 6250$ at different instants spanning half of one temporal oscillation: isosurface of $Q = 0.1$ and streamlines. The four chosen times correspond to the dash-point lines in Fig. 22.

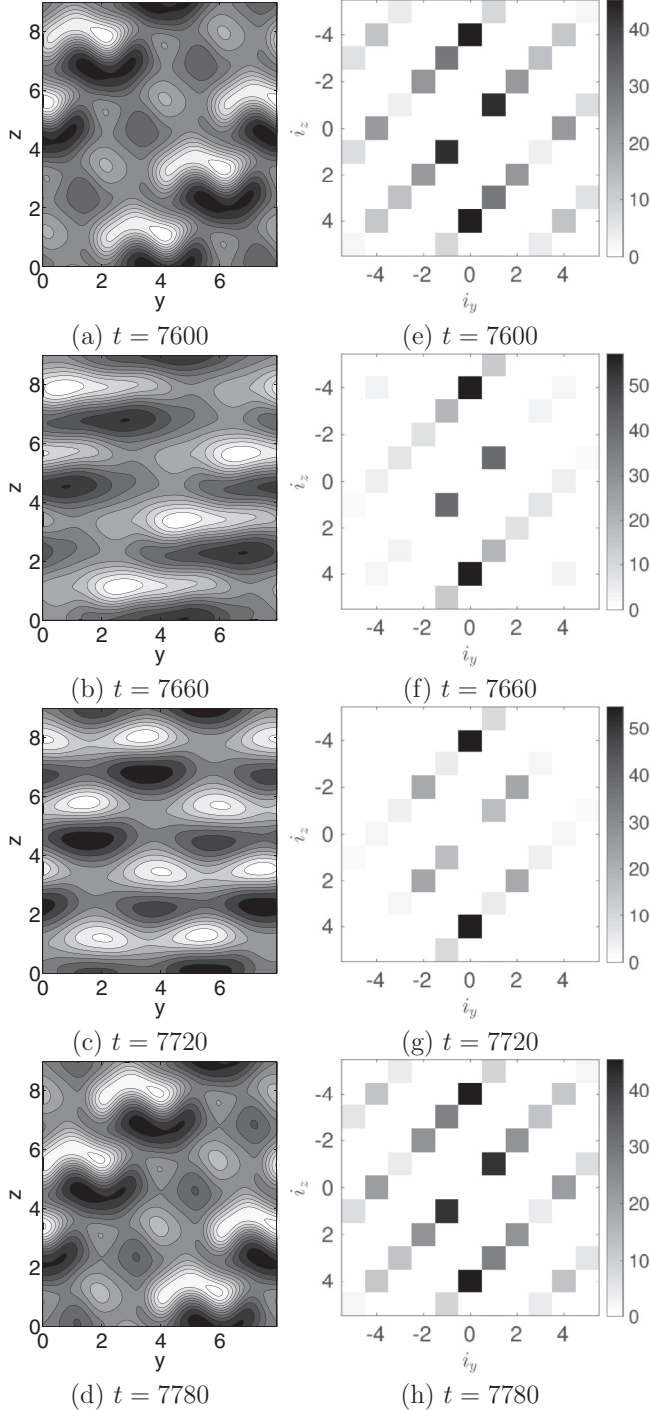


FIG. 21. Evolution at $Ra = 6250$. Left: Temperature contours at $Ra = 6250$ on a vertical plane $x = 0.0381$ for four different times (indicated in Fig. 20). Right: Corresponding spatial spectrum of the temperature perturbation $|\Delta\hat{\theta}(i_y, i_z)|$ ($i_y, i_z = -5, 5$).

mode $\hat{\theta}(1,3)$ represent, respectively, 84.87 and 7.37% of the variance of the thermal fluctuations, so that these four modes together capture 92.24% of the variance.

The temporal evolution of the principal modes $\hat{\theta}(0,4)$, $\hat{\theta}(2,2)$, and $\hat{\theta}(1,1)$ is shown in Fig. 22. All three amplitudes oscillate periodically with different phases. The mode $\hat{\theta}(0,4)$ corresponding to the primary rolls has the largest amplitude.

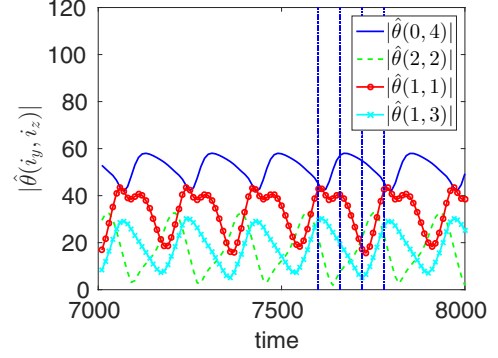


FIG. 22. Temporal evolution at $Ra = 6250$ of the four most energetic spectral coefficients $|\hat{\theta}(i_y, i_z)|$ on the plane $x = 0.0381$. The vertical dash-point lines correspond to the four instants shown in Fig. 21.

The mode $\hat{\theta}(1,1)$ corresponding to instability mechanism C has the second largest amplitude. The mode $\hat{\theta}(1,3)$ has almost the same amplitude as the mode $\hat{\theta}(2,2)$.

D. $Ra \geq 6300$: Temporal chaos

When Ra is increased to $Ra = 6300$, the flow becomes temporally chaotic, as evidenced by the temperature time series at the point $(0.0381, 0.122, 4.96)$ in Fig. 23(a). Figure 23(b) shows that the temporal Fourier spectrum of the signal corresponding to $t \in [5000, 8000]$ is broadband and nearly continuous. Figure 24 confirms that the evolution of the flow structure is more complex. At times $t = 7200, 7320$, and 7600 [Figs. 24(a), 24(c) and 24(f)], the distortion of the rolls is mild, while at times $t = 7270$ and 7400 the deformation is stronger, characterized by both roll waviness and roll thinning (defects). Pattern A can occasionally be dominant [see, for instance, Fig. 24(e)].

Figure 25(a) shows the time-averaged 2D Fourier coefficients of the temperature $\langle |\hat{\theta}(i_y, i_z)| \rangle$ on the vertical plane $x = 0.0381$ (the average is taken over the times $t \in [7000, 8000]$). The three most energetic modes are still $\hat{\theta}(0,4)$, $\hat{\theta}(2,2)$, and $\hat{\theta}(1,1)$, which represent 78.75% of the variance of the thermal fluctuations. Together with the mode $\hat{\theta}(1,3)$, the four modes capture 87.81% of the total perturbation energy. This confirms that the spatial organization of the flow is still dominated by the few wave numbers corresponding to the most unstable eigenmodes of linear stability analysis. However, the temporal evolution of these four principal modes is chaotic, as shown in Fig. 25(b).

VI. CONCLUSION

The goal of this paper is to examine the instabilities of the natural convection in a fluid layer between vertical plates maintained at different temperatures. In the first part of the paper, linear stability analysis and nonlinear integration are used to study the evolution of steady 2D corotating rolls, which represent the primary bifurcation of the conduction solution. While nonlinear integration requires several hundreds of hours on a parallel computer, linear stability analysis based on an Arnoldi method requires only tens of minutes on a single-processor machine, and therefore constitutes a cheap,

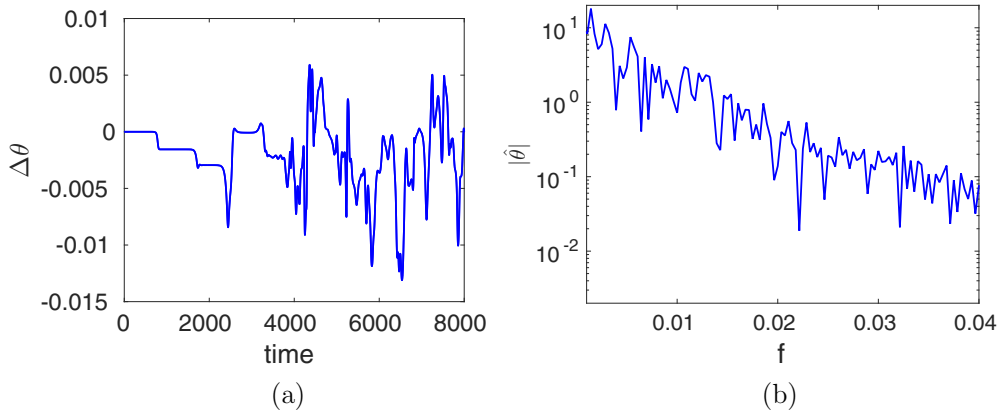


FIG. 23. (a) Time series of temperature perturbation at the point (0.0381, 0.122, 4.96) in the boundary layer near the hot wall, $Ra = 6300$. (b) Temporal spectrum of the chaotic portion of the signal in (a) limited to $t \in [5000, 8000]$.

efficient investigation tool, which provides a more accurate description of the most unstable patterns than standard Fourier analysis. Results indicate that the 2D rolls are unstable to two kinds of 3D steady disturbances: one corresponding to a local pairing of the rolls (“wavy roll,” instability A) and the other consisting of localized roll thinning (“defective or broken roll,” instability C).

We find that the critical spanwise number and the corresponding eigenmode are very sensitive to the exact value of

the roll size associated with the vertical wave number k_z , and that the critical Rayleigh numbers associated with the two different mechanisms are close to each other. This results in a competition between the two mechanisms in the full simulation. For a vertical plate aspect ratio of $A_z = 9$, we found that the disturbance eigenmode predicted by linear stability analysis (mode A) was in fact only a transient feature, leading to a steady asymptotic nonlinear state which was a mixture of modes A and C.

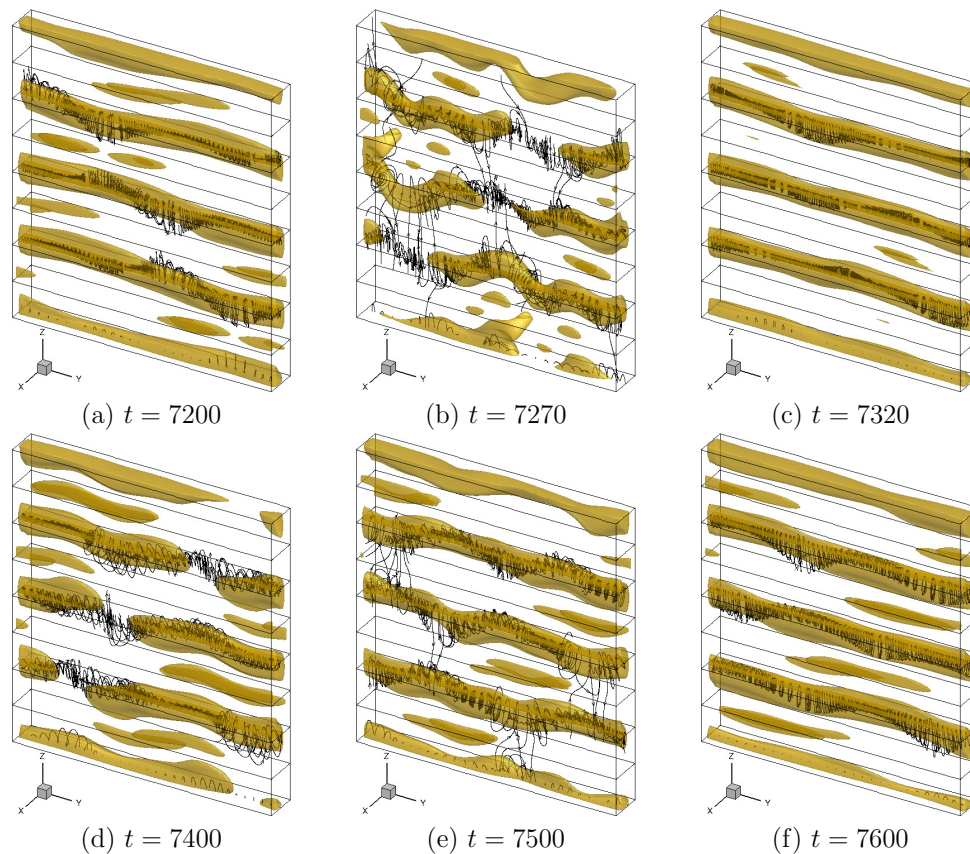


FIG. 24. Flow structures at $Ra = 6300$ for six different instants [indicated by vertical dash-point lines in Fig. 25 (right)]: isosurface of $Q = 0.1$ and streamlines.

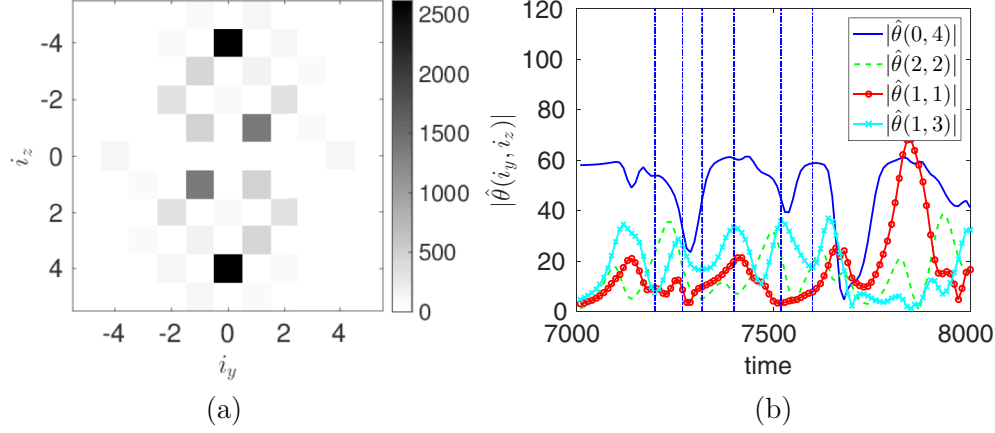


FIG. 25. Temperature field at $Ra = 6300$ (the spatial average has been removed). (a) Time-averaged 2D Fourier coefficient of the temperature $|\hat{\theta}(i_y, i_z)|$ ($i_y, i_z = -5, 5$) on the vertical plane $x = 0.0381$; the average is performed over times $t \in [7000, 8000]$. (b) Temporal evolution of the four most energetic spectral coefficients $|\hat{\theta}(i_y, i_z)|$ on the plane $x = 0.0381$. The vertical dash-point lines correspond to the six instances of the flow pattern shown in Fig. 24.

In the second part of the paper, successive bifurcations were determined from the nonlinear simulation as the Rayleigh number was increased. The 3D steady flow associated with the mixed mode becomes time dependent at $Ra = 6150$ through a Hopf bifurcation. After a period-doubling bifurcation the flow becomes temporally chaotic at $Ra = 6300$, i.e., at a Rayleigh number which is less than 10% higher than the critical Rayleigh number of the primary bifurcation. A notable result is that at the onset of chaos the flow still consists of rolls characterized by the two local deformations patterns predicted by linear stability theory: vortex pairing and roll thinning. This highlights the complementary role of linear stability analysis and nonlinear simulation.

ACKNOWLEDGMENTS

This work was granted access to the HPC (High Performance Computing) resources of IDRIS (Institute for Development and Resources in Intensive Scientific Computing) under the allocations 2013-2a0326 and 2014-2a0326 of GENCI (Grand Équipement National De Calcul Intensif). We thank the anonymous referees for providing valuable comments which helped us improve the manuscript.

APPENDIX: ARNOLDI METHOD

We now give a description of the Arnoldi method.

The stability of the base flow $[U(x, z), V = 0, W(x, z), \Theta(x, z)]$ with respect to a 3D perturbation $[u(x, y, z), v(x, y, z), w(x, y, z), \theta(x, y, z)]$ can be tested by integrating the linearized 3D unsteady Navier-Stokes equations, which take the following form:

$$\begin{aligned} \frac{\partial u}{\partial x} + \frac{\partial v}{\partial y} + \frac{\partial w}{\partial z} &= 0, \\ \frac{\partial u}{\partial t} + U \frac{\partial u}{\partial x} + W \frac{\partial u}{\partial z} + u \frac{\partial U}{\partial x} + w \frac{\partial W}{\partial z} &= -\frac{\partial p}{\partial x} \\ &+ \frac{\text{Pr}}{\sqrt{\text{Ra}}} \left(\frac{\partial^2 u}{\partial x^2} + \frac{\partial^2 u}{\partial y^2} + \frac{\partial^2 u}{\partial z^2} \right), \end{aligned}$$

$$\begin{aligned} \frac{\partial v}{\partial t} + U \frac{\partial v}{\partial x} + W \frac{\partial v}{\partial z} &= -\frac{\partial p}{\partial y} + \frac{\text{Pr}}{\sqrt{\text{Ra}}} \left(\frac{\partial^2 v}{\partial x^2} + \frac{\partial^2 v}{\partial y^2} + \frac{\partial^2 v}{\partial z^2} \right), \\ \frac{\partial w}{\partial t} + U \frac{\partial w}{\partial x} + W \frac{\partial w}{\partial z} + u \frac{\partial W}{\partial x} + w \frac{\partial W}{\partial z} &= -\frac{\partial p}{\partial z} \\ &+ \frac{\text{Pr}}{\sqrt{\text{Ra}}} \left(\frac{\partial^2 w}{\partial x^2} + \frac{\partial^2 w}{\partial y^2} + \frac{\partial^2 w}{\partial z^2} \right) + \text{Pr}\theta, \\ \frac{\partial \theta}{\partial t} + U \frac{\partial \theta}{\partial x} + W \frac{\partial \theta}{\partial z} + u \frac{\partial \Theta}{\partial x} + w \frac{\partial \Theta}{\partial z} &= \frac{1}{\sqrt{\text{Ra}}} \left(\frac{\partial^2 \theta}{\partial x^2} + \frac{\partial^2 \theta}{\partial y^2} + \frac{\partial^2 \theta}{\partial z^2} \right). \end{aligned} \quad (\text{A1})$$

Equations (A1) can be integrated directly to obtain the unstable disturbance patterns. However, in view of the periodic boundary conditions, we can suppose that the 3D perturbation takes a periodic form as $u(x, z, t) \cos(k_y y)$, $v(x, z, t) \sin(k_y y)$, $w(x, z, t) \cos(k_y y)$, $\theta(x, z, t) \cos(k_y y)$, where k_y is the wave number in the y direction. With this assumption of periodicity for the perturbations, Eq. (A1) becomes

$$\begin{aligned} \frac{\partial u}{\partial x} + k_y y + \frac{\partial w}{\partial z} &= 0, \\ \frac{\partial u}{\partial t} + U \frac{\partial u}{\partial x} + W \frac{\partial u}{\partial z} + u \frac{\partial U}{\partial x} + w \frac{\partial W}{\partial z} &= -\frac{\partial p}{\partial x} + \frac{\text{Pr}}{\sqrt{\text{Ra}}} \left(\frac{\partial^2 u}{\partial x^2} + \frac{\partial^2 u}{\partial z^2} - k_y^2 u \right), \\ \frac{\partial v}{\partial t} + U \frac{\partial v}{\partial x} + W \frac{\partial v}{\partial z} &= -\frac{\partial p}{\partial y} + \frac{\text{Pr}}{\sqrt{\text{Ra}}} \left(\frac{\partial^2 v}{\partial x^2} + \frac{\partial^2 v}{\partial z^2} - k_y^2 v \right), \\ \frac{\partial w}{\partial t} + U \frac{\partial w}{\partial x} + W \frac{\partial w}{\partial z} + u \frac{\partial W}{\partial x} + w \frac{\partial W}{\partial z} &= -\frac{\partial p}{\partial z} + \frac{\text{Pr}}{\sqrt{\text{Ra}}} \left(\frac{\partial^2 w}{\partial x^2} + \frac{\partial^2 w}{\partial z^2} - k_y^2 w \right) + \text{Pr}\theta, \\ \frac{\partial \theta}{\partial t} + U \frac{\partial \theta}{\partial x} + W \frac{\partial \theta}{\partial z} + u \frac{\partial \Theta}{\partial x} + w \frac{\partial \Theta}{\partial z} &= \frac{1}{\sqrt{\text{Ra}}} \left(\frac{\partial^2 \theta}{\partial x^2} + \frac{\partial^2 \theta}{\partial z^2} - k_y^2 \theta \right). \end{aligned} \quad (\text{A2})$$

Boundary conditions for Eqs. (A1) and (A2) are of Dirichlet type and homogeneous.

Suppose now $(U, 0, W)$ and (u, v, w) verifying the incompressibility condition, with the following notations: $\mathbf{X} = (U, 0, W, \Theta)$, $\mathbf{x} = (u, v, w, \theta)$, L represents the 2D Laplace operator, N represents the advection terms and the linear buoyancy term, and $N_{\mathbf{x}}$ is the Fréchet derivative of N on \mathbf{X} . We can recast Eq. (A2) into the following compact form:

$$\frac{\partial \mathbf{x}}{\partial t} = \left[\frac{C}{\sqrt{\text{Ra}}} (L - k^2 I) + N_{\mathbf{x}} \right] \mathbf{x} = J_{\mathbf{x}} \mathbf{x} \quad (\text{A3})$$

where $J_{\mathbf{x}}$ is the Jacobian and constant C is equal to 1 for θ and equal to Pr for velocities.

The Arnoldi method has been used in several studies to study hydrodynamic instability, as, for instance, for natural convection in a rectangular cavity [30] or spherical Couette flow [38].

To determine whether the perturbation \mathbf{x} in Eq. (A3) grows or decreases with respect to time t , we need to compute the eigenvalues of the Jacobian $J_{\mathbf{x}}$. However, the dimension of the discretized Navier-Stokes equation system is so large that we cannot compute these eigenvalues exactly, due to the available computing resources. Therefore, we used the Arnoldi method, which provides approximates for them. The Arnoldi iteration relies on the orthogonalization of a Krylov subspace to provide a series of Hessenberg matrices which approximate $J_{\mathbf{x}}$. The eigenvalues of these Hessenberg matrices constitute the Ritz eigenvalues. In most circumstances the eigenvalues converge to some of the eigenvalues of $J_{\mathbf{x}}$ (typically the leading ones). The convergence rate of the procedure is not fully understood yet in the general case.

After applying a mixed implicit-explicit scheme to Eq. (A3) and some algebraic calculations [30,31,38], we can show that if the time step Δt is sufficiently small then

$$\mathbf{x}^{n+1} \approx \exp(\Delta t J_{\mathbf{x}}) \mathbf{x}^n. \quad (\text{A4})$$

Therefore, we can compute the iterative action of $J_{\mathbf{x}}$ on a given vector (an initial flow state) to form the Krylov subspace by successive time stepping of the linearized Navier-Stokes system (A2).

If Δt stays small enough, we can extend Eq. (A4) to $\mathbf{x}^{n+K} = \exp(\Delta t J_{\mathbf{x}}) \mathbf{x}^{n+K-1} = \dots = \exp(K \Delta t J_{\mathbf{x}}) \mathbf{x}^n$. Therefore, the series $\mathbf{x}^{n+K}, \mathbf{x}^{n+2K}, \dots, \mathbf{x}^{n+lK}$ is an approximation of a series $\exp(K \Delta t J_{\mathbf{x}}) \mathbf{x}^n, \exp(2K \Delta t J_{\mathbf{x}}) \mathbf{x}^n, \dots, \exp[(l-1)K \Delta t J_{\mathbf{x}}] \mathbf{x}^n$, which forms a Krylov subspace. We can obtain a general relation as following:

$$\begin{aligned} & (\mathbf{x}^{n+K}, \mathbf{x}^{n+2K}, \dots, \mathbf{x}^{n+lK}) \\ & \approx \exp(K \Delta t J_{\mathbf{x}}) (\mathbf{x}^n, \mathbf{x}^{n+K}, \mathbf{x}^{n+2K}, \dots, \mathbf{x}^{n+(l-1)K}). \end{aligned} \quad (\text{A5})$$

This relation shows that $(\mathbf{x}^{n+K}, \mathbf{x}^{n+2K}, \dots, \mathbf{x}^{n+lK})$ can be considered as a multiplication of operator $\exp(K \Delta t J_{\mathbf{x}})$ on the Krylov subspace $(\mathbf{x}^n, \mathbf{x}^{n+K}, \mathbf{x}^{n+2K}, \dots, \mathbf{x}^{n+(l-1)K})$.

Supposing that $q^0, q^1, q^2, \dots, q^{l-1}$ and q^l is the orthonormal basis of the Krylov subspace spanned by $\mathbf{x}^n, \mathbf{x}^{n+K}, \mathbf{x}^{n+2K}, \dots, \mathbf{x}^{n+(l-1)K}$ and \mathbf{x}^{n+lK} , the Gram-Schmidt orthonormalization procedure can give us not only an orthonormal basis $q^0, q^1, q^2, \dots, q^{l-1}$ and q^l but also QR factorization of the Krylov subspace spanned by $\mathbf{x}^n, \mathbf{x}^{n+K}, \mathbf{x}^{n+2K}, \dots, \mathbf{x}^{n+(l-1)K}$

and \mathbf{x}^{n+lK} . Therefore, we have

$$\begin{aligned} & (\mathbf{x}^n, \mathbf{x}^{n+K}, \mathbf{x}^{n+2K}, \dots, \mathbf{x}^{n+(l-1)K}, \mathbf{x}^{n+lK}) \\ & = (q^0, q^1, q^2, \dots, q^{l-1}, q^l) R = QR \end{aligned} \quad (\text{A6})$$

and

$$\begin{aligned} & (\mathbf{x}^n, \mathbf{x}^{n+K}, \mathbf{x}^{n+2K}, \dots, \mathbf{x}^{n+(l-1)K}) \\ & = (q^0, q^1, q^2, \dots, q^{l-1}) \tilde{R} = \tilde{Q} \tilde{R} \end{aligned} \quad (\text{A7})$$

where \tilde{Q} contains the first l columns of Q and \tilde{R} is a l -order submatrix of R . Compared to Eq. (A7), Eq. (A6) has one more column and one more line. If we drop the first column of Eq. (A6) and use the relation Eq. (A5), we get

$$\begin{aligned} & \exp(K \Delta t J_{\mathbf{x}}) (\mathbf{x}^n, \mathbf{x}^{n+K}, \mathbf{x}^{n+2K}, \dots, \mathbf{x}^{n+(l-1)K}) \\ & = (q^0, q^1, q^2, \dots, q^{l-1}, q^l) \bar{R} = Q \bar{R} \end{aligned} \quad (\text{A8})$$

where \bar{R} is the submatrix of R with its first column omitted, which has dimension $(l+1) \times l$. As the last line of \bar{R} has only one nonzero term, the diagonal one, denoted $r_{l,l}$, we can recast the relation (A8) as following:

$$\begin{aligned} & \exp(K \Delta t J_{\mathbf{x}}) (\mathbf{x}^n, \mathbf{x}^{n+K}, \mathbf{x}^{n+2K}, \dots, \mathbf{x}^{n+(l-1)K}) \\ & = (q^0, q^1, q^2, \dots, q^{l-1}) \tilde{\mathbf{H}} + r_{l,l} q^l = \tilde{Q} \tilde{\mathbf{H}} + \bar{c} q^l. \end{aligned} \quad (\text{A9})$$

Here the Hessenberg matrix $\tilde{\mathbf{H}}$ represents the first l lines of \bar{R} . If \bar{c} is small enough, we have

$$\exp(K \Delta t J_{\mathbf{x}}) \tilde{Q} \tilde{R} = \tilde{Q} \tilde{\mathbf{H}} \quad (\text{A10})$$

which can be recast as $\exp(K \Delta t J_{\mathbf{x}}) \tilde{Q} = \tilde{Q} \tilde{\mathbf{H}} \tilde{R}^{-1}$. As \tilde{R} and \tilde{R}^{-1} are upper triangular matrices, $\tilde{\mathbf{H}} \tilde{R}^{-1}$ is still a Hessenberg matrix, which is noted as \mathbf{H} . So we get the following relation:

$$\exp(K \Delta t J_{\mathbf{x}}) (q^0, q^1, q^2, \dots, q^{l-1}) = (q^0, q^1, q^2, \dots, q^{l-1}) \mathbf{H} \quad (\text{A11})$$

or simply $\exp(K \Delta t J_{\mathbf{x}}) \tilde{Q} = \tilde{Q} \mathbf{H}$

If \mathbf{H} is diagonalizable, then $\mathbf{H} = S \Lambda S^{-1}$, where Λ is the diagonal matrix containing the spectrum of \mathbf{H} and S is the matrix formed by the eigenvectors of \mathbf{H} . So we have $\exp(K \Delta t J_{\mathbf{x}}) \tilde{Q} = \tilde{Q} S \Lambda S^{-1}$, then

$$\exp(K \Delta t J_{\mathbf{x}}) \tilde{Q} S = \tilde{Q} S \Lambda, \quad (\text{A12})$$

which shows that Λ , the spectrum of \mathbf{H} , corresponds to the spectrum of the matrix $\exp(K \Delta t J_{\mathbf{x}})$, and $\tilde{Q} S$ corresponds to the eigenvectors of $\exp(K \Delta t J_{\mathbf{x}})$. Therefore, the leading eigenvalues of \mathbf{H} can give us those of $\exp(K \Delta t J_{\mathbf{x}})$, which can be easily done by using the library LAPACK.

We use the Arnoldi iteration to compute approximate eigenvalues of the Jacobian matrix $J_{\mathbf{x}}$ using successive time stepping of the linearized Navier-Stokes equations (A2). In practice, the linearized unsteady Navier-Stokes equations (A2) are integrated for a few dozen time steps in order to generate a Krylov subspace. Then the Gram-Schmidt orthonormalization method is applied to construct the Hessenberg matrix \mathbf{H} . Once \mathbf{H} obtained, its leading eigenvalues can be calculated by using the library LAPACK. This procedure should be repeated in a time loop to determine the appropriate dimension of the Krylov subspace and the moment to stop the time integration. The monotonic decrease of the residual \bar{c} , which appears as the last term in Eq. (A9), serves as a criterion to stop the time integration.

- [1] G. K. Batchelor, Heat transfer by free convection across a closed cavity between vertical boundaries at different temperatures, *Quart. Appl. Math* **12**, 209 (1954).
- [2] J. W. Elder, Laminar free convection in a vertical slot, *J. Fluid Mech.* **23**, 77 (1965).
- [3] A. E. Gill and A. Davey, Instability of a buoyancy-driven system, *J. Fluid Mech.* **35**, 775 (1969).
- [4] R. F. Bergholz, Instability of steady natural convection in a vertical fluid layer, *J. Fluid Mech.* **84**, 743 (1978).
- [5] J. Mizushima and K. Gotoh, Nonlinear evolution of the disturbance in a natural convection induced in a vertical fluid layer, *J. Phys. Soc. Jpn.* **52**, 1206 (1983).
- [6] J. Mizushima and Y. Saito, Equilibrium characteristics of the secondary convection in a vertical fluid layer between two flat plates, *Fluid Dyn. Res.* **2**, 183 (1987).
- [7] J. Mizushima, Equilibrium solution of the secondary convection in a vertical fluid layer between two flat plates, *Fluid Dyn. Res.* **5**, 289 (1990).
- [8] D. W. Ruth, On the transition to transverse rolls in an infinite vertical fluid layer—a power series solution, *Int. J. Heat Mass Transfer* **22**, 1199 (1979).
- [9] P. G. Daniels and M. Weinstein, Nonlinear stability of convective flow between heated vertical planes, *J. Eng. Math.* **23**, 377 (1989).
- [10] C. M. Vest and V. S. Arpaci, Stability of natural convection in a vertical slot, *J. Fluid Mech.* **36**, 1 (1969).
- [11] Y. Oshima, Experimental studies of free convection in a rectangular cavity, *J. Phys. Soc. Jpn.* **30**, 872 (1971).
- [12] D. R. Chenoweth and S. Paolucci, Gas flow in vertical slots with large horizontal temperature differences, *Phys. Fluids* **28**, 2365 (1985).
- [13] P. Le Quéré, A note on multiple and unsteady solutions in a tall cavity, *ASME J. Heat Transfer* **112**, 965 (1990).
- [14] S. Xin, *Simulation Numérique de Convection Naturelle Turbulente*, Ph.D. thesis, Université Paris VI, 1993.
- [15] S. Xin and P. Le Quéré, Direct numerical simulation of two-dimensional chaotic natural convection in a differentially heated cavity of aspect ratio 4, *J. Fluid Mech.* **304**, 87 (1995).
- [16] J. R. Phillips, Direct simulations of turbulent unstratified natural convection in a vertical slot for $Pr=0.71$, *Int. J. Heat Mass Transfer* **39**, 2485 (1996).
- [17] J. Mizushima and H. Tanaka, Transition routes of natural convection in a vertical fluid layer, *Phys. Fluids* **14**, 21 (2002).
- [18] J. M. Cornet and C. H. Lamarque, Nonlinear behavior of the instability of steady natural convection in a vertical air layer, *Mech. Res. Comm.* **24**, 179 (1997).
- [19] J. Tao and F. Zhuang, Absolute and convective instabilities of the natural convection in a vertical heated slot, *Phys. Rev. E* **62**, 7957 (2000).
- [20] B. Lartigue, S. Lorente, and B. Bourret, Multicellular natural convection in a high aspect ratio cavity: Experimental and numerical results, *Int. J. Heat Mass Transfer* **43**, 3157 (2000).
- [21] A. Y. Gelfgat, Time-dependent modeling of oscillatory instability of three-dimensional natural convection of air in a laterally heated cubic box, *Theor. Comput. Fluid Dyn.* **31**, 447 (2017).
- [22] O. Sánchez, I. Mercader, O. Batiste, and A. Alonso, Natural convection in a horizontal cylinder with axial rotation, *Phys. Rev. E* **93**, 063113 (2016).
- [23] M. Nagata and F. H. Busse, Three-dimensional tertiary motions in a plane shear layer, *J. Fluid Mech.* **135**, 1 (1983).
- [24] A. Chait and S. A. Korpela, The secondary flow and its stability for natural convection in a tall vertical enclosure, *J. Fluid Mech.* **200**, 189 (1989).
- [25] R. M. Clever and F. H. Busse, Tertiary and quaternary solutions for convection in a vertical fluid layer heated from the side, Chaos, Solitons, *Fractals* **5**, 1795 (1995).
- [26] J. L. Wright, H. Jin, K. G. T. Hollands, and D. Naylor, Flow visualization of natural convection in a tall, air-filled vertical cavity, *Int. J. Heat Mass Transfer* **49**, 889 (2006).
- [27] Z. Gao, A. Sergent, B. Podvin, S. Xin, P. Le Quéré, and L. S. Tuckerman, Transition to chaos of natural convection between two infinite differentially heated vertical plates, *Phys. Rev. E* **88**, 023010 (2013).
- [28] A. Cimarelli and D. Angeli, Routes to chaos of natural convection flows in vertical channels, *Int. Commun. Heat Mass Transfer* **81**, 201 (2017).
- [29] A. Bejan, *Convection Heat Transfer* (Wiley, New York, 1985).
- [30] S. Xin and P. Le Quéré, Linear stability analysis of natural convection flows in a differentially heated square cavity with conducting horizontal walls, *Phys. Fluids* **13**, 2529 (2001).
- [31] S. Xin, Instabilité de convection naturelle en cavité et méthodes numériques adaptées, lecture note of 11e École de printemps de Mécanique des Fluides Numériques, Oléron, France, June 7–13th, 2009 (unpublished).
- [32] S. Xin, J. Chergui, and P. Le Quéré, 3D spectral parallel multi-domain computing for natural convection flows, in *Parallel Computational Fluid Dynamics 2008*, edited by D. Tromeur-Dervout, G. Brenner, D. R. Emerson, and J. Erhel, Lecture Notes in Computational Science and Engineering Vol. 74 (Springer, Berlin, 2011), pp. 163–171.
- [33] J. C. R. Hunt, A. A. Wray, and P. Moin, *Eddies, Streams, and Convergence Zones in Turbulent Flows*, in Proceedings of the 1988 Summer Program (SEE N89-24538 18-34), pp. 193–208.
- [34] R. D. Henderson and D. Barkley, Secondary instability in the wake of a circular cylinder, *Phys. Fluids* **8**, 1683 (1996).
- [35] L. Tuckerman, *Practical Bifurcation Techniques and Nonlinear Tourism*, Lecture Notes, Dynamique Non-Linéaire (Université Pierre et Marie Curie, Paris, France).
- [36] C. Ho and P. Huerre, Perturbed free shear layers, *Ann. Rev. Fluid Mech.* **16**, 365 (1984).
- [37] Z. Gao, A. Sergent, B. Podvin, and S. Xin, Chaotic dynamics of a convection roll in a highly confined, vertical, differentially heated fluid layer, *Phys. Rev. E* **91**, 013006 (2015).
- [38] C. K. Mamun and L. S. Tuckerman, Asymmetry and Hopf bifurcation in spherical Couette flow, *Phys. Fluids* **7**, 80 (1995).